Science of Remote Sensing 2 (2020) 100012

Contents lists available at ScienceDirect

Science of Remote Sensing

journal homepage: www.journals.elsevier.com/science-of-remote-sensing

Full Length Article

Water property in high-altitude Qinghai Lake in China

Wei Shi [a,b,*], Menghua Wang [a], Junsheng Li [c]

[a] NOAA National Environmental Satellite, Data, and Information Service, Center for Satellite Applications and Research, E/RA3, 5830 University Research Court, College Park, MD 20740, USA
[b] CIRA at Colorado State University, Fort Collins, CO, 80523, USA
[c] AIRI, Chinese Academy of Sciences, Beijing, 100094, PR China

ARTICLE INFO

Keywords:
High altitude lakes
Qinghai Lake
Remote sensing
Water optical property
Tibetan plateau
VIIRS

ABSTRACT

Qinghai Lake in China, which is located at an altitude of 3260 m, is the highest inland lake among the 50 largest lakes in the world. Therefore, satellite measurement of water quality is the most important and feasible tool for routinely assessing the water property and its variations in Qinghai Lake. We derive the normalized water-leaving radiance spectra $nL_w(\lambda)$ in Qinghai Lake from measurements of the Visible Infrared Imaging Radiometer Suite (VIIRS), after accurately computing the top-of-atmosphere Rayleigh radiances in the satellite Level-1 to Level-2 ocean color data processing. Satellite-derived $nL_w(\lambda)$ spectra, chlorophyll-a (Chl-a) concentration, and the water diffuse attenuation coefficient at 490 nm, $K_d(490)$, in the period of 2012–2018 are used to evaluate and understand the dynamics of water properties in Qinghai Lake. Results show that VIIRS-measured $nL_w(\lambda)$ spectra match quite well with the in situ data, e.g., the mean and median ratios of the VIIRS-derived and in situ-measured $nL_w(\lambda)$ at 443 nm are 0.9741 and 0.9898, respectively. Enhanced $nL_w(\lambda)$ at 486 nm and 551 nm can be observed from satellite-derived $nL_w(\lambda)$ spectra for the entire lake. VIIRS-derived $nL_w(\lambda)$ spectra show significant seasonal cycles. High $nL_w(\lambda)$ values occur in July while low values occur in April. Results also show the seasonal and interannual changes of Chl-a and $K_d(490)$ in Qinghai Lake. Low Chl-a and $K_d(490)$ are normally observed in April, and they typically peak in the early summer. Peculiarly, however, anomaly high values in Chl-a and $K_d(490)$ occurred in June 2016. The analysis of empirical orthogonal functions (EOFs) shows the dominant modes for Chl-a and $K_d(490)$ are interannual modes that account for about 79.1% and 31.5% of the their total variances, respectively. The second EOF mode for Chl-a and $K_d(490)$ shows the seasonal changes, and contributes to about 6.1% and 14.0% of their respective total variances.

1. Introduction

China's Qinghai Lake, also known as Koko Nor, is an alkaline lake in the Tibetan Plateau with a surface elevation of 3260 m (Fig. 1). As the largest lake in China, Qinghai Lake covers ~4300 km^2. It is the highest altitude inland lake among the largest 50 lakes in the world. The depth of the lake averages about 21 m. There are five permanent streams providing about 80% of the total water influx.

After the lake separated from the Yellow River approximately 150,000 years ago, the salinity of the lake has increased. The salinity of the lake is about 14 practical salinity units (psu) and the PH value is about 9.3 (Zhang et al., 2015). As the most important riverine process, the carbonate weathering led to the dominance of Ca^{2+} and dissolved inorganic carbon (DIC) in the river and groundwater (Jin et al., 2010). Both Na^+ and Cl^- are the major ion sources in Qinghai Lake. Since the 1960s, concentrations of NH_4^+ and NO_3^- increased significantly due to increased human activities (Ao et al., 2014). Over the past 600 years, the fluctuations of the water level in Qinghai Lake more or less corresponded to the wet and dry stages (Feng et al., 2000).

Climate change has a big influence on the areal variation of Qinghai Lake (Tang et al., 2018). During the last several decades, the increased rate of the global surface temperature is ~0.2 °C/decade (Hansen et al., 2010). The upward trend in surface temperature in the Tibetan Plateau is almost twice that of the global warming rate (Xu et al., 2008). In the nearby Qinghai Lake region, the average temperature increased about 0.319 °C per decade in the past 50 years, and 0.415 °C per decade from 2005–2016. The Qinghai Lake area decreased by ~2% in the period of 1987–2005, and increased ~3% from 2006–2016 (Tang et al., 2018). Precipitation is found to be the primary factor for the change in the Qinghai Lake area. Indeed, precipitation is responsible for about 93% of the water level variations (Fang et al., 2019).

In Qinghai Lake, studies of the water quality, e.g., the lake's physical,

* Corresponding author. NOAA/NESDIS/STAR, 20740, USA.
E-mail address: wei.1.shi@noaa.gov (W. Shi).

https://doi.org/10.1016/j.srs.2020.100012
Received 26 May 2020; Received in revised form 1 September 2020; Accepted 10 November 2020
Available online 28 November 2020

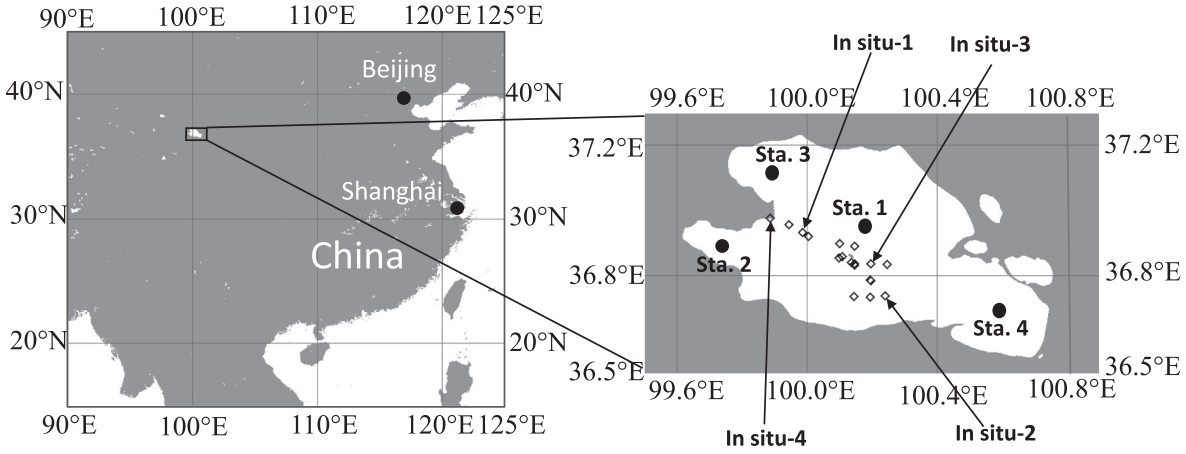

Fig. 1. Qinghai Lake and the 18 locations for the in situ $nL_w(\lambda)$ measurements (marked as squares). The comparisons between VIIRS retrievals and field measurements in Fig. 2 are conducted at the location of (a) In situ-1 [36.928°N, 99.989°E], (b) In situ-2 [36.735°N, 100.244°E], (c) In situ-3 [36.830°N, 100.198°E], and (d) In situ-4 [36.973°"N, 99.890°E]. Four pseudo-stations at Station 1 [36.95°N, 100.16°E], Station 2 [36.90°N, 99.73°E], Station 3 [37.13°N, 99.89°E], and Station 4 [36.71°N, 100.57°E] are also noted to further examine VIIRS-measured $nL_w(\lambda)$ spectra.

Table 1
In situ measurement time and locations.

No	Date	Beijing Time	Longitude (°E)	Latitude (°N)
1	8/23/2014	10:03	99.9462778	36.955833
2	8/23/2014	10:30	99.9889722	36.931667
3	8/23/2014	10:57	100.007056	36.919538
4	8/23/2014	12:07	100.138972	36.83909
5	8/23/2014	12:35	100.111194	36.856372
6	8/23/2014	13:03	100.102194	36.897333
7	8/23/2014	13:41	100.149028	36.889064
8	8/23/2014	14:37	100.101306	36.852103
9	8/24/2014	11:14	100.149333	36.831128
10	8/24/2014	11:35	100.197944	36.785359
11	8/24/2014	12:12	100.243528	36.736141
12	8/24/2014	12:42	100.198	36.733974
13	8/24/2014	13:05	100.14725	36.734244
14	8/24/2014	13:45	100.199472	36.783744
15	8/24/2014	14:16	100.248111	36.833821
16	8/24/2014	14:40	100.198278	36.834744
17	8/24/2014	15:05	100.149167	36.83409
18	8/24/2014	16:35	99.8899444	36.974859

optical, biological, biogeochemical, and ecosystem processes (from either field surveys, aerial sensing, or satellite remote sensing), are sparse in comparison to those in other sea-level lakes such as Lake Taihu. Due to increasing concentrations of nitrogen and silica, the lake water transparency has decreased compared to historical data in the 1960s (Ao et al., 2014). In addition, lake optical properties have been measured and reported (Cen et al., 2013; Wang et al., 2005), phytoplankton features were analyzed (Yao et al., 2011; Zhu et al., 2016), and the absorption spectral features of the dissolved and particulate matters in Qinghai Lake were also studied (Zhou et al., 2005).

The water level and coverage of Qinghai Lake were evaluated with satellite remote sensing. The lake level dropped ~2 m between 1975 and 2000, and the coverage of the lake dropped by ~150 km^2 (Shen and Kuang, 2002). Satellite altimetry measurements were also examined for the lake's water level and its temporal change (Zhang et al., 2011a, 2011b). The lake surface topography was measured and evaluated (Li et al., 2018). Observations from the Moderate Resolution Imaging Spectroradiometer (MODIS) were studied and monitored for surface temperatures in Qinghai Lake (Wan et al., 2017; Xiao et al., 2013). In addition, the frozen duration was also monitored with satellite passive microwave remote sensing (Che et al., 2009).

Satellite observations such as MODIS and the Visible Infrared Imaging Radiometer Suite (VIIRS) onboard the Suomi National Polar-orbiting Partnership (SNPP) have proven to effectively monitor lake environmental changes such as algae bloom and water clarity (El-Habashi et al., 2016; Shi et al., 2019). High quality water optical data are produced after atmospheric correction in the ocean color data processing (Gordon and Wang, 1994; Wang, 2007; Wang and Shi, 2007). Satellite-derived $nL_w(\lambda)$ spectra can then be used to produce a variety of water biological and biogeochemical products in order to study various physical and bio-optical processes in inland waters. Specifically, the water quality and water turbidity were characterized with MODIS observations (Wang et al., 2011, 2012). The cyanobacteria blooms were assessed and evaluated (Hu et al., 2010), and sediment concentration dynamics (Shi et al., 2018) in global inland lakes like Lake Taihu were also studied.

However, most of these studies are for global sea-level inland waters because inaccurate atmospheric correction over high-altitude waters can lead to a significant underestimation of $nL_w(\lambda)$ retrievals (Wang, 2016; Wang et al., 2020a). Thus, satellite-derived $nL_w(\lambda)$ spectra and subsequent products have significant errors in the satellite ocean color products from MODIS and VIIRS, etc. Specifically, top-of-atmosphere (TOA) Rayleigh scattering radiances for a high-altitude lake surface are calculated at sea-level, thus the TOA Rayleigh scattering radiance computations over the high-altitude lakes were overestimated. This led to biased low (even negative) $nL_w(\lambda)$ spectral retrievals (Wang, 2016).

In this study, new Rayleigh lookup tables (LUTs) (Wang, 2016) were generated and used in order to derive accurate $nL_w(\lambda)$ spectra for high-altitude Qinghai Lake. In a recent study, we demonstrated that high quality $nL_w(\lambda)$ retrievals can be obtained from VIIRS observations for high-altitude Lake Tahoe with an elevation of 1897 m (Wang et al., 2020a). VIIRS-derived $nL_w(\lambda)$ spectra match in-situ data quite well over Lake Tahoe. The mean and median of ratios of the VIIRS-SNPP versus in-situ $nL_w(\lambda)$ for the blue and green bands are 0.999 and 1.002. Other lake parameters such as Secchi depth (SD) can also be derived and used to further evaluate the long-term lake environment in Lake Tahoe (Wang et al., 2020a).

There are two purposes for this study. First, a comparison between the VIIRS-derived $nL_w(\lambda)$ spectra and in situ measurements is conducted to show the performance of the newly implemented Rayleigh LUTs over the high-altitude Qinghai Lake. In addition to the comparison and validation efforts in Lake Tahoe, this can provide further evaluations of the satellite-derived $nL_w(\lambda)$ in the high-altitude Qinghai Lake, which has a much higher elevation, and is situated deeper into the continent than Lake Tahoe. Because Qinghai Lake is the highest altitude lake of the world's

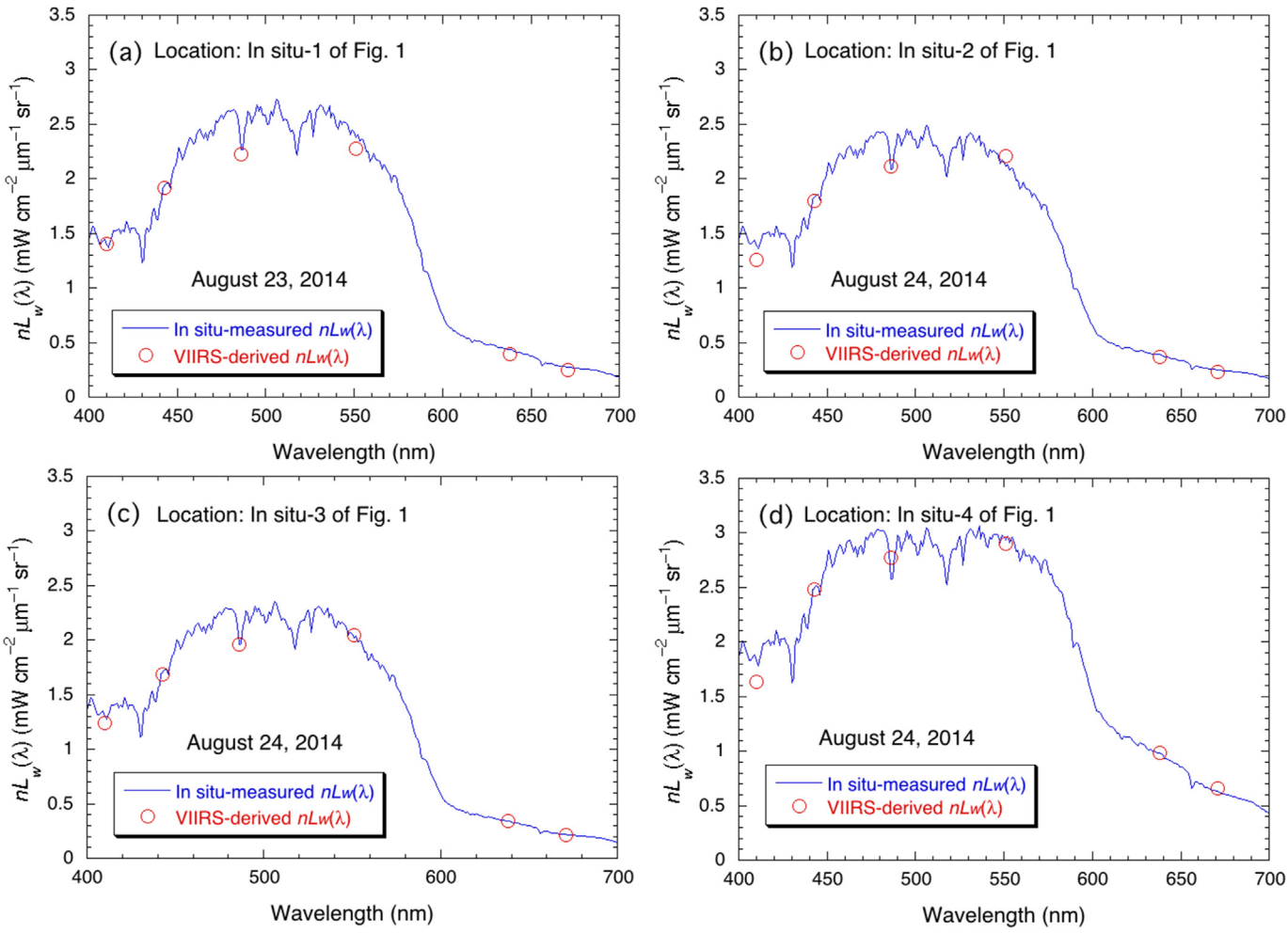

Fig. 2. Satellite-derived and in situ-measured $nL_w(\lambda)$ at locations of (a) In situ-1, (b) In situ-2, (c) In situ-3, and (d) In situ-4.

major lakes, validation results in combination with the previous Lake Tahoe study (Wang et al., 2020a) shall provide comprehensive evaluations and evidence of the VIIRS-derived $nL_w(\lambda)$ data quality for global high-altitude lakes, in particular, the sub-alpine lakes to the alpine lakes over the Tibetan Plateau. Second, Qinghai Lake has been much less studied in comparison to other sea-level lakes like Lake Taihu (Wang et al., 2011). In this study, VIIRS-SNPP-derived water optical properties, such as $nL_w(\lambda)$ spectra, are characterized and quantified in the period of 2012–2018. The variabilities of these water optical properties are evaluated and analyzed. In addition, the Empirical Orthogonal Function (EOF) analysis is also carried out to further decompose the variations of the lake properties and it possibly provides the driving forces and processes for these variabilities in Qinghai Lake.

2. Satellite-derived $nL_w(\lambda)$ data in Qinghai Lake

2.1. VIIRS $nL_w(\lambda)$ spectra retrievals

As a data continuity mission for MODIS, VIIRS-SNPP provides Earth observation data for the atmosphere, land, cryosphere, and ocean (Goldberg et al., 2013). Detailed descriptions about the sensor specification, data processing procedure, algorithms, and products related to satellite ocean color can be found in Wang et al. (2013a).

The TOA radiance $L_t(\lambda)$ measured by a satellite ocean color sensor like VIIRS is composed of the TOA Rayleigh radiance $L_r(\lambda)$ from atmosphere molecular scattering, $L_a(\lambda)$ from the aerosol scattering, and $L_w(\lambda)$ from the water body (Gordon and Wang, 1994; IOCCG, 2010; Wang, 2007). Rayleigh radiance $L_r(\lambda)$ is normally the dominant component of $L_t(\lambda)$ in the visible bands, especially for the blue bands (Gordon and Wang, 1994; IOCCG, 2010; Wang, 2007). Thus, it is critical to accurately compute Rayleigh spectral radiances $L_r(\lambda)$ for global inland lakes.

In this study, new Rayleigh radiance LUTs (Wang, 2016) were applied in order to calculate $nL_w(\lambda)$ using the Multi-Sensor Level-1 to Level-2 (MSL12) ocean color data processing system for global waters including the high-altitude Qinghai Lake. It is noted that MSL12 is NOAA's official VIIRS ocean color data processing system (Wang et al., 2013a,b), which was developed in the late 1990s for satellite data processing for multiple ocean color sensors (Wang and Franz, 2000; Wang et al., 2002). The new and improved Rayleigh radiance computation accounts for the sensor spectral response function and the variations of lake surface atmospheric pressure (Wang, 2016). The changes of atmospheric pressure from the standard water surface atmospheric pressure over Qinghai Lake are included in the TOA Rayleigh radiance estimation. With the new and improved TOA Rayleigh radiance computations, VIIRS-derived $nL_w(\lambda)$ over Qinghai Lake are produced from the observations between 2012 and 2018. VIIRS-SNPP-derived $nL_w(\lambda)$ spectra over the lake are evaluated and validated using the in situ $nL_w(\lambda)$ data.

2.2. In situ-measured $nL_w(\lambda)$ spectra

During the period between August 23-24, 2014, a field campaign was conducted in Qinghai Lake to measure the remote sensing reflectance spectra $R_{rs}(\lambda)$. A SVC GER1500 field spectrometer (350–1050 nm with a spectral resolution of 3 nm) was used to measure the lake surface

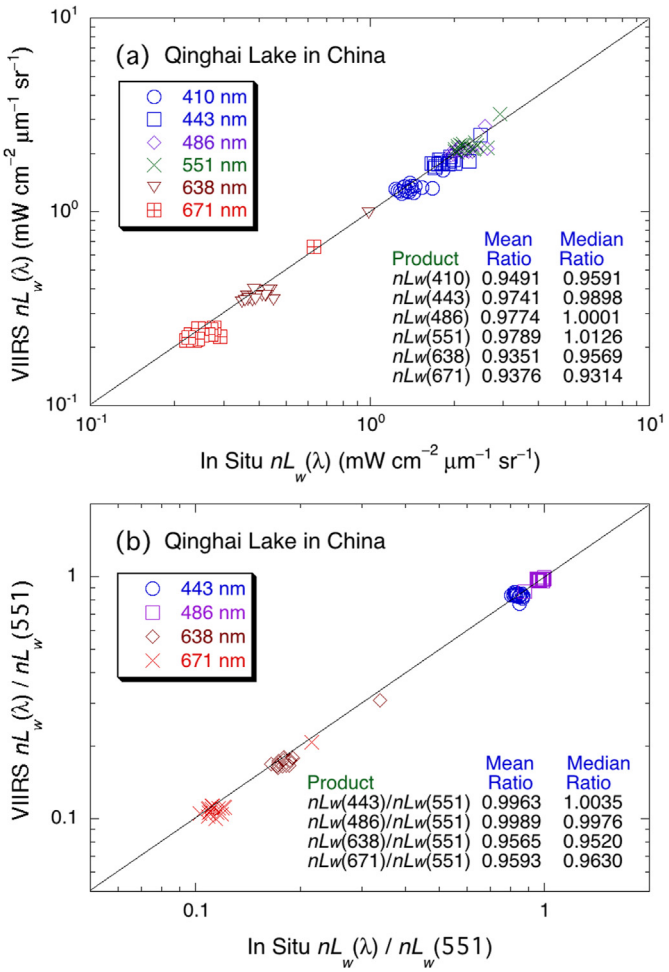

Fig. 3. (a) Satellite-derived $nL_w(\lambda)$ vs. in situ $nL_w(\lambda)$ at the various VIIRS spectral bands and (b) VIIRS-SNPP-derived $nL_w(\lambda)/nL_w(551)$ vs. in situ $nL_w(\lambda)/nL_w(551)$ at the various VIIRS spectral bands.

reflectance spectra following the "above water method". At each sampling station in the campaign, the reflectance spectra of a Labsphere Spectralon grey panel ($L_p(\lambda)$), skylight ($L_{sky}(\lambda)$), and water surface ($L_{sw}(\lambda)$), were measured on the ship. Then, $R_{rs}(\lambda)$ spectra were computed with the following equation (Lee et al., 2002):

$$R_{rs}(\lambda) = \frac{L_{sw}(\lambda)}{\pi L_p(\lambda)/\rho_p(\lambda)} - \frac{r_{sky} L_{sky}(\lambda)}{\pi L_p(\lambda)/\rho_p(\lambda)} - \Delta. \quad (1)$$

In Eq. (1), r_{sky} can be determined by the Fresnel formula. Δ is a spectrally constant bias, which can be estimated by using the assumption that $R_{rs}(\lambda)$ near 900 nm is 0 for relatively clear water like Qinghai Lake.

The in situ $R_{rs}(\lambda)$ spectra were converted to $nL_w(\lambda)$ spectra in order to evaluate the performance of VIIRS-derived $nL_w(\lambda)$ spectra over the lake. The in situ measurements at the 18 stations as shown in Fig. 1 were taken. Of the 18 in situ measurements (Table 1), eight measurements were carried out on August 23, 2014, and 10 measurements on August 24, 2014. In addition to in situ $R_{rs}(\lambda)$ spectra, suspended particulate matter (SPM) concentration and SD data were also measured at each station. In Qinghai Lake, in situ SPM data were ~6–8 mg/L and SD values were ~2–4 m at these stations.

3. Results

3.1. Evaluation of VIIRS-derived $nL_w(\lambda)$

In the period between August 23-24, 2014, VIIRS measurements on August 24 were cloud free in Qinghai Lake, while the in situ sites in the lake were covered by clouds on August 23. To evaluate and validate satellite $nL_w(\lambda)$ retrievals, we set up a 5×5 box that co-locates with each in situ data site, and the median value of $nL_w(\lambda)$ in the box is calculated and then used to compare against the corresponding in situ $nL_w(\lambda)$ data. Considering the limited in situ measurements and the typically low day-to-day variability of $nL_w(\lambda)$ for the lake, no time restriction was used for the VIIRS and in situ $nL_w(\lambda)$ matchup comparison.

Fig. 2 provides some comparison results of $nL_w(\lambda)$ spectra at the in situ-1 station (Fig. 2a), in situ-2 station (Fig. 2b), in situ-3 station (Fig. 2c), and in situ-4 station (Fig. 2d). Note that the locations for the in

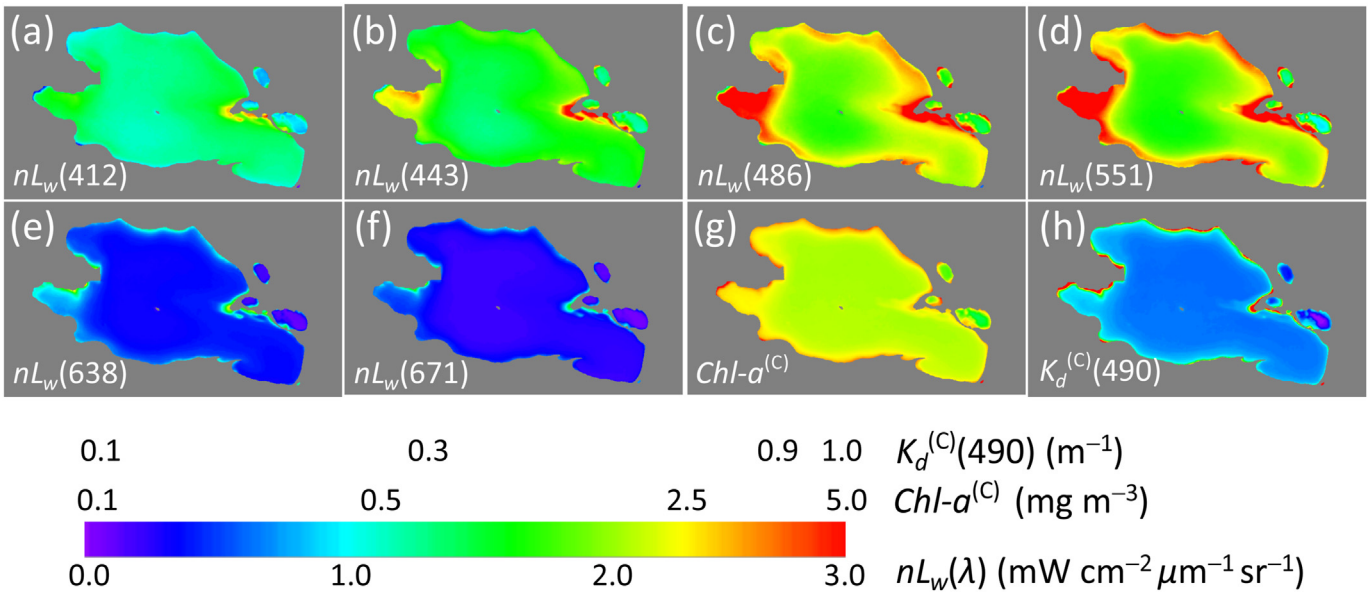

Fig. 4. Satellite-derived/calculated climatology (2012–2018) water properties in Qinghai Lake for (a) $nL_w(410)$, (b) $nL_w(443)$, (c) $nL_w(486)$, (d) $nL_w(551)$, (e) $nL_w(638)$, (f) $nL_w(671)$, (g) Chl-a$^{(C)}$, and (h) $K_d^{(C)}(490)$.

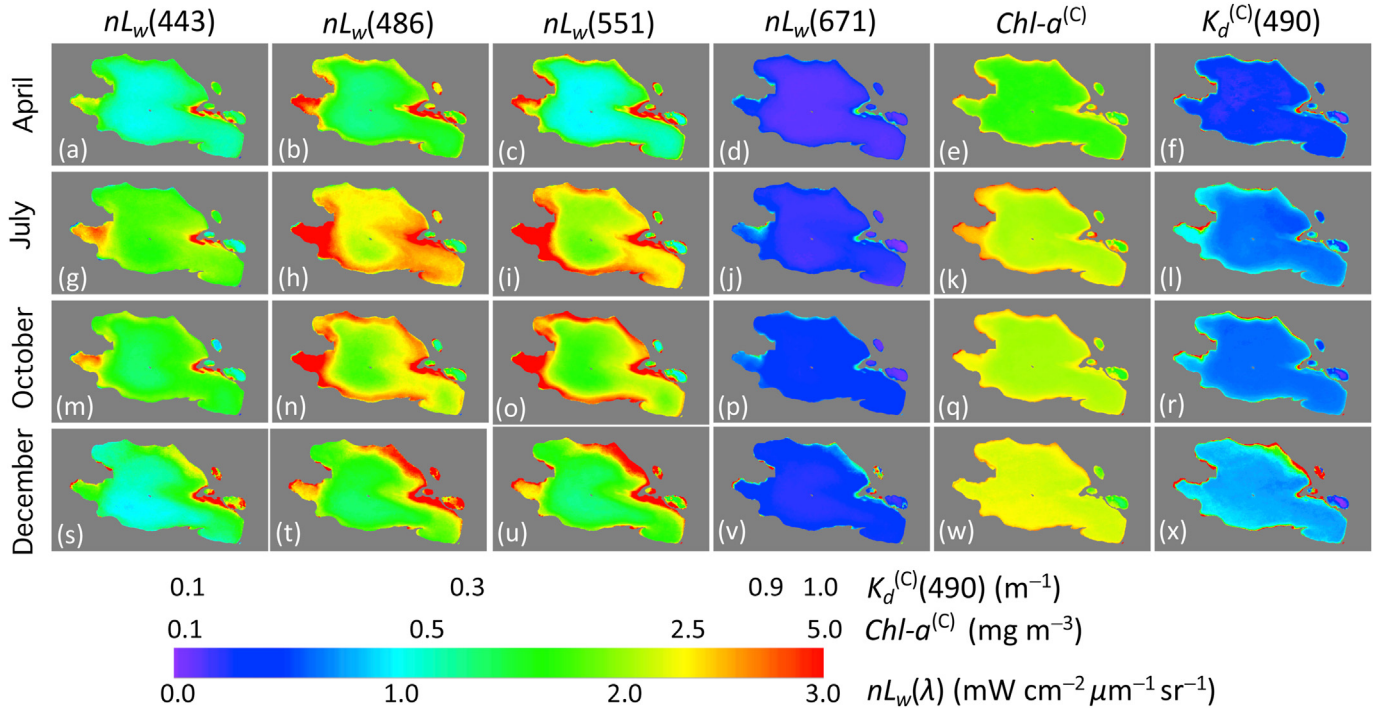

Fig. 5. Satellite-derived water properties in Qinghai Lake with different seasons for products of (along the row) nL_w(443), nL_w(486), nL_w(551), nL_w(671), Chl-$a^{(C)}$, and $K_d^{(C)}$(490) in the month of (a–f) April, (g–l) July, (m–r) October, and (s–x) December.

situ-1 to in situ-4 stations are marked in Fig. 1b and the field measurement at the in situ-1 and VIIRS observation were not on the same day.

VIIRS-derived $nL_w(\lambda)$ spectra agree well with in situ measurements (Fig. 2). Specifically, VIIRS-derived $nL_w(\lambda)$ values are all consistent with the in situ $nL_w(\lambda)$ for these cases (Fig. 2). It is also noted that $nL_w(\lambda)$ spectra from both satellite and in situ measurements at these stations peak in the wavelength range between 470–550 nm. Indeed, waters in Qinghai Lake are typical productive inland waters. These comparison results demonstrate that VIIRS-derived $nL_w(\lambda)$ spectra using the new improved TOA Rayleigh radiance computations over the high-altitude Qinghai Lake are generally accurate.

Fig. 3 further quantifies the accuracy of VIIRS $nL_w(\lambda)$ at all 18 stations in Qinghai Lake. For $nL_w(\lambda)$ (wavelengths at 410, 443, 486, 551, 638, and 671 nm), VIIRS-SNPP-derived $nL_w(\lambda)$ values all agree well with the in situ measurements even though the time difference between the two has been relaxed. Specifically, mean $nL_w(\lambda)$ ratios of these two $nL_w(\lambda)$ at the various VIIRS bands are 0.9491, 0.9741, 0.9774, 0.9789, 0.9351, and 0.9376, respectively. In addition, the corresponding median ratios are 0.9591, 0.9898, 1.0001, 1.0126, 0.9569, and 0.9314, respectively. Figs. 2 and 3 show that $nL_w(\lambda)$ retrievals over Qinghai Lake are of high data quality. Therefore, the subsequent lake water parameters e.g., chlorophyll-a (Chl-a) concentration, water diffuse attenuation coefficient at 490 nm, K_d(490), can be derived with the inputs of the VIIRS-SNPP-derived $nL_w(\lambda)$ spectra.

The Chl-a concentration in waters can be computed with $nL_w(\lambda)$ ratios at the blue and green bands, i.e., $nL_w(551)/nL_w(443)$ or $nL_w(551)/nL_w(486)$ (O'Reilly et al., 1998) from satellite observations. Similarly, K_d(490) can be derived from the radiance ratio of $nL_w(551)/nL_w(443)$ for the open ocean and less turbid lake waters (Wang et al., 2009). Recently, Yu et al. (2019) developed a new algorithm to calculate SPM concentration with the ratios of $nL_w(\lambda)$ at the green, red, and near-infrared (NIR) wavelengths for all water types (Yu et al., 2019). Considering that many ocean color products are related to the radiance ratio $nL_w(\lambda)/nL_w(551)$, we further evaluate the performance of this ratio from VIIRS measurements in comparison with those from the in situ data. Fig. 3b shows that the mean ratios of $nL_w(\lambda)/nL_w(551)$ for the VIIRS bands of 443, 486, 638, and 671 nm are 0.9963, 0.9989, 0.9565, and 0.9593, respectively, while the corresponding median ratios are 1.0035, 0.9976, 0.9520, and 0.9630, respectively.

3.2. Variations of $nL_w(\lambda)$, Chl-$a^{(C)}$, and $K_d^{(C)}$(490) in Qinghai Lake

We define the VIIRS-calculated Chl-a and K_d(490) from the input of $nL_w(\lambda)$ spectra using the ocean color index (OCI) Chl-a algorithm (Hu et al., 2012; Wang and Son, 2016) and the K_d(490) algorithm (Wang et al., 2009) as Chl-$a^{(C)}$ and $K_d^{(C)}$(490). Because there is a lack of in situ Chl-a and K_d(490) field data for validating the corresponding VIIRS-derived products over Qinghai Lake, we focus in this study on the variations of VIIRS-calculated Chl-$a^{(C)}$ and $K_d^{(C)}$(490) over the lake rather than their true values. Therefore, VIIRS-derived/calculated $nL_w(\lambda)$, Chl-$a^{(C)}$, and $K_d^{(C)}$(490) can be used to study water properties and evaluate their seasonal, spatial, and long-term variations over Qinghai Lake.

Most of Qinghai Lake is covered with ice in the months of January, February, and March, thus the climatology ocean color product maps from VIIRS-SNPP are derived using the data gathered in April–December from 2012 to 2018. Fig. 4 provides the climatology imageries of nL_w(410) (Fig. 4a), nL_w(443) (Fig. 4b), nL_w(486) (Fig. 4c), nL_w(551) (Fig. 4d), nL_w(638) (Fig. 4e), and nL_w(671) (Fig. 4f), as well as Chl-$a^{(C)}$ (Fig. 4g) and $K_d^{(C)}$(490) (Fig. 4h). It is noted that the climatology values of Chl-$a^{(C)}$ and $K_d^{(C)}$(490) in each pixel are computed as the median values of all the satellite retrievals from 2012–2018.

Similar to the spectral feature at the in situ stations (Fig. 2), $nL_w(\lambda)$ peaks at 486 nm (Fig. 4c) and 551 nm (Fig. 4d). Elevated nL_w(486) and nL_w(551) can be found in the coastal region, especially in the southwestern bay region with nL_w(486) and nL_w(551) over ~3 mW cm^{-2} μm^{-1} sr^{-1}. In this region, increased nL_w(638) (Fig. 4e) and nL_w(671) (Fig. 4f) can also be found. In comparison to the climatology maps of nL_w(486) and nL_w(551), the spatial distribution of nL_w(412) (Fig. 4a) is generally uniform in Qinghai Lake.

The climatology map of Chl-$a^{(C)}$ (Fig. 4g) shows less spatial variability in the lake. In fact, the climatology Chl-$a^{(C)}$ values range between ~1.6–2.5 mg m^{-3}. This implies that the Chl-a distribution in the lake is

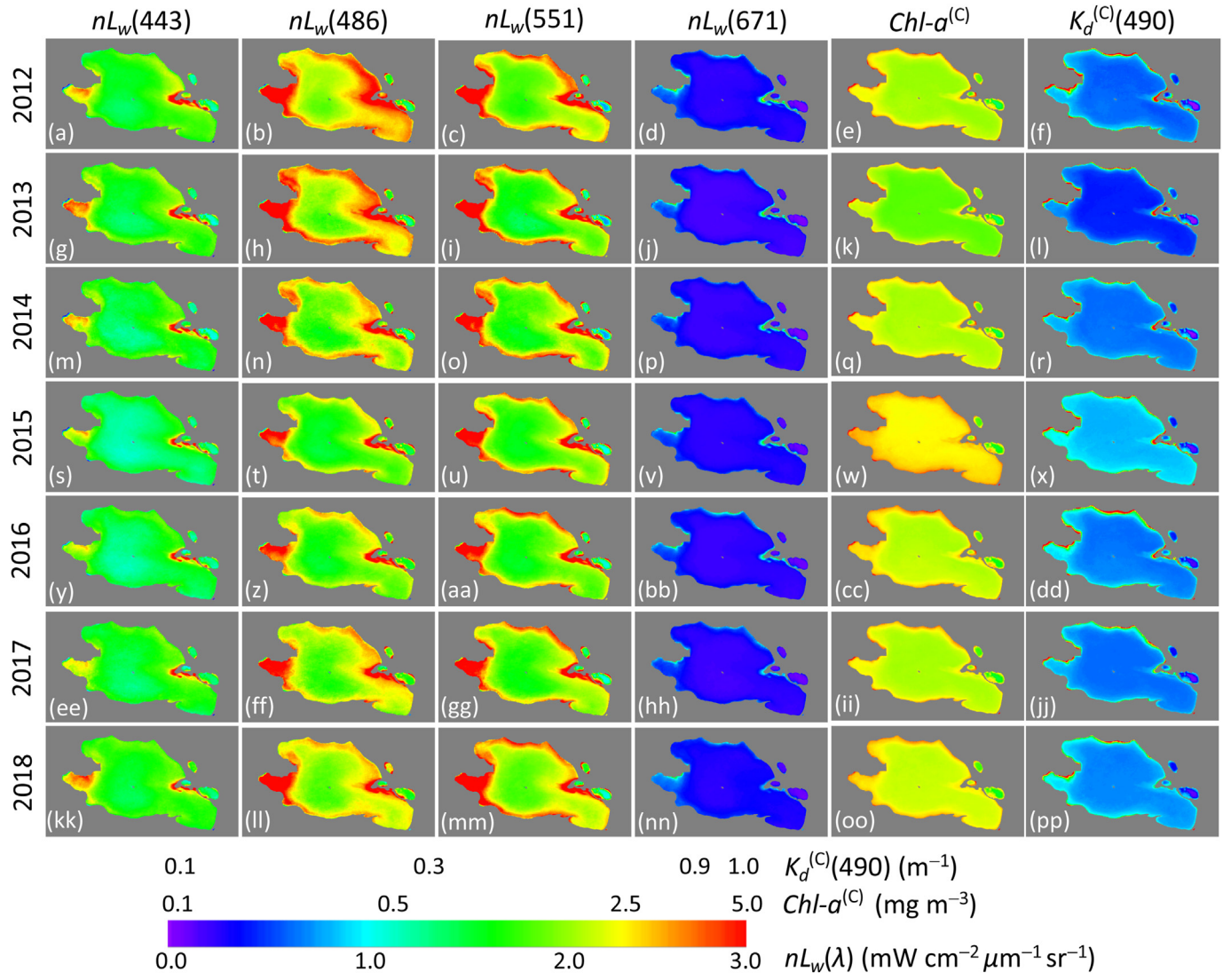

Fig. 6. Satellite-derived/calculated interannual maps of water properties in Qinghai Lake for $nL_w(443)$, $nL_w(486)$, $nL_w(551)$, $nL_w(671)$, Chl-a$^{(C)}$, and $K_d^{(C)}(490)$ in the year of (a–f) 2012, (g–l) 2013, (m–r) 2014, (s–x) 2015, (y–dd) 2016, (ee–jj) 2017, and (kk–pp) 2018.

more or less uniform even though both climatology maps of $nL_w(443)$ (Fig. 4b) and $nL_w(551)$ (Fig. 4d) show some notable spatial differences. In comparison to the climatology map of Chl-a$^{(C)}$, the spatial variability of the climatology $K_d^{(C)}(490)$ (Fig. 4h) is also insignificant. For most of Qinghai Lake, $K_d^{(C)}(490)$ is ~0.16 m^{-1}. It can reach ~0.20 m^{-1} in the southwestern bay region. This also suggests that the SPM concentration in the southwestern bay region is the highest in the lake.

Seasonal changes of $nL_w(\lambda)$ spectra, Chl-a$^{(C)}$, and $K_d^{(C)}(490)$ in Qinghai Lake are shown in Fig. 5. Since most of the lake is covered with ice in the months of January, February, and March, the seasonal changes of $nL_w(\lambda)$, Chl-a$^{(C)}$, and $K_d^{(C)}(490)$ are presented in April (for spring) (Fig. 5a–5f), July (for summer) (Fig. 5g–5l), October (for autumn) (Fig. 5m–5r), and December (for winter) (Fig. 5s–5x). For $nL_w(\lambda)$ spectra, they reach their peaks in July (Fig. 5g–5j) and October (Fig. 5m–5p), while the minimum $nL_w(\lambda)$ values occur in April (Fig. 5a–5d).

The seasonal patterns of Chl-a$^{(C)}$ and $K_d^{(C)}(490)$ are obviously different from those of $nL_w(\lambda)$. Specifically, the highest Chl-a$^{(C)}$ occurs in December (Fig. 5w) and the lowest in April (Fig. 5e). In comparison to the less significant seasonal change of Chl-a$^{(C)}$ in Qinghai Lake, $K_d^{(C)}(490)$ shows notable seasonal variations. $K_d^{(C)}(490)$ peaks in December with values over ~0.25–0.30 m^{-1} (Fig. 5x). The minimal $K_d^{(C)}(490)$ occurs in April (Fig. 5l) with values of ~0.1–0.15 m^{-1} in most of the lake.

Fig. 6 shows the interannual variations of $nL_w(\lambda)$ at the VIIRS bands of 443, 486, 551, and 671 nm, as well as Chl-a$^{(C)}$ and $K_d^{(C)}(490)$ from VIIRS observations from 2012–2018. In general, moderately enhanced $nL_w(\lambda)$ can be found in the years of 2012, 2013, and 2018. This is especially true for $nL_w(486)$ (Fig. 6b, 6h, 6n, 6t, and 6ll). However, $nL_w(551)$ in these seven years do not show wide temporal changes (Fig. 6c, 6i, 6o, 6u, 6aa, 6gg, and 6mm). Both Chl-a$^{(C)}$ (Fig. 6e, 6k, 6q, 6w, 6cc, 6ii, and 6oo) and $K_d^{(C)}(490)$ (Fig. 6f, 6l, 6r, 6x, 6dd, 6jj, and 6pp) had notable interannual variations between 2012–2018. For Chl-a$^{(C)}$, the peak occurred in 2015 (Fig. 6w), and the minimum values were in 2013 (Fig. 6k). The highest $K_d^{(C)}(490)$ was observed in 2015 (Fig. 6x) and the lowest was in 2013 (Fig. 6l). These results show that the interannual variation of Chl-a in Qinghai Lake is mostly in phase with that of $K_d^{(C)}(490)$.

Seasonal and interannual variations in $nL_w(\lambda)$ spectra for Qinghai Lake are evaluated (Fig. 7). The seasonal change in $nL_w(\lambda)$ spectra in the lake is significant (Fig. 7a). All of the seasonal $nL_w(\lambda)$ spectra peak at 486 nm. Specifically, all $nL_w(\lambda)$ values reach the highest in July and the lowest in April. In July, $nL_w(486)$ reaches ~2.5 mW cm^{-2} μm^{-1} sr^{-1} (Fig. 7a), while in April $nL_w(486)$ is ~1.5 mW cm^{-2} μm^{-1} sr^{-1}. The $nL_w(\lambda)$ spectrum in the month of October is similar to the climatology spectrum. However, the interannual differences in $nL_w(\lambda)$ over Qinghai Lake (Fig. 7b) are smaller than the seasonal $nL_w(\lambda)$ variations. VIIRS-derived $nL_w(486)$ data

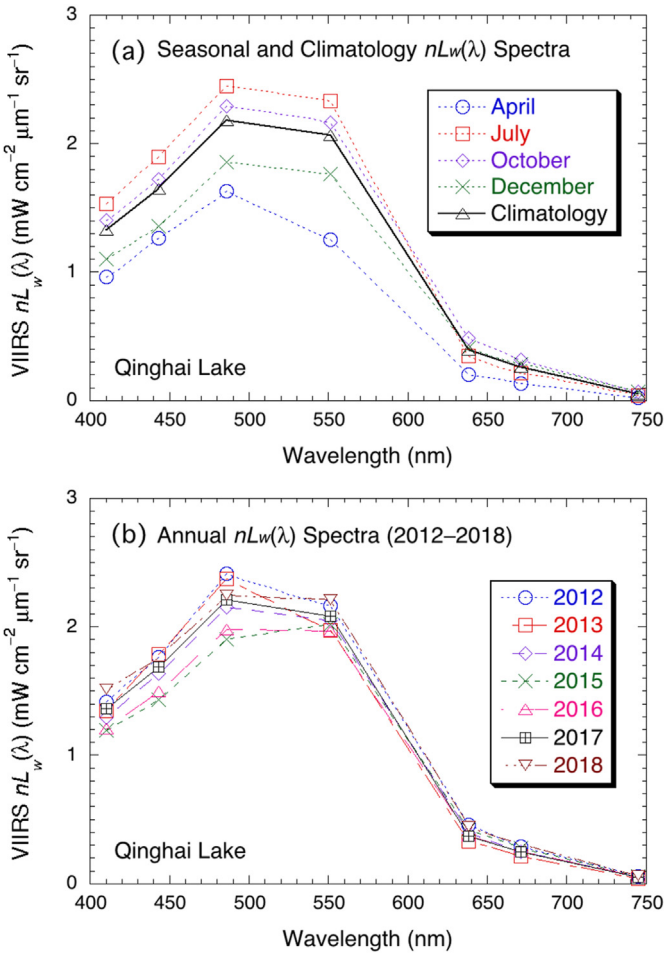

Fig. 7. Satellite-derived $nL_w(\lambda)$ spectra in Qinghai Lake for (a) the climatology (2012–2018) and monthly means in April, July, October, and December, and (b) annual means from 2012 to 2018.

show the largest interannual variability. As shown in the $nL_w(\lambda)$ maps between 2012–2018 (Fig. 6), $nL_w(\lambda)$ spectra were the highest in 2012 and 2013, while the lowest $nL_w(\lambda)$ spectra occurred in 2015 and 2016.

Fig. 8 further shows the characterization results of the seasonal $nL_w(\lambda)$ spectra at the different lake locations of Station 1 (Fig. 8a), Station 2 (Fig. 8b), Station 3 (Fig. 8c), and Station 4 (Fig. 8d). The locations of pseudo (or assigned) Stations 1–4 in the lake are noted in Fig. 1b. Except for Station 2, VIIRS-derived $nL_w(\lambda)$ spectra in the other three stations are similar in $nL_w(\lambda)$ magnitudes, their spectral shapes, and seasonal variations. At these three stations, $nL_w(\lambda)$ peaks at 486 nm and in the month of July. The lowest $nL_w(\lambda)$ values in the three stations are found in April. At Station 2, the seasonal change of $nL_w(\lambda)$ spectra is significant (Fig. 8b). The peak of the $nL_w(\lambda)$ spectrum occurs at 551 nm in July. In contrast, the peak of the lowest $nL_w(\lambda)$ spectrum occurs at 486 nm in December (Fig. 8b). Note that the magnitude of $nL_w(\lambda)$ spectra at Station 2 are overall higher than those in the other three stations with the peak $nL_w(551)$ at ~4.0 mW cm^{-2} μm^{-1} sr^{-1} in July (Fig. 8b). At Stations 1, 3, and 4, however, the maximum $nL_w(486)$ value is only ~2.5 mW cm^{-2} μm^{-1} sr^{-1} in July.

Fig. 9 details the temporal changes of $nL_w(\lambda)$, Chl-$a^{(C)}$, and $K_d^{(C)}(490)$ for the entire Qinghai Lake. In the period between 2012–2018, $nL_w(\lambda)$ show clear seasonality (Fig. 9a) as well as interannual variability. The variations of all $nL_w(\lambda)$ at different wavelengths are in phase with each other (Fig. 9a). As identified in Figs. 5 and 7a, $nL_w(\lambda)$ reached the peak amount in summer and lowest in early spring. On the other hand, the interannual variations of $nL_w(\lambda)$ in Fig. 7b also show that $nL_w(\lambda)$ were high in 2012 and 2013 and low in 2015 and 2016. The result agrees with the $nL_w(\lambda)$ maps in the corresponding years in Fig. 6.

The time series of Chl-$a^{(C)}$ for the entire lake between 2012–2018 is shown in Fig. 9b. As observed in the maps of Chl-$a^{(C)}$ (Fig. 5), seasonal variability for Chl-$a^{(C)}$ shows two peaks in June and December. The interannual changes of Chl-$a^{(C)}$ showed anomalous Chl-$a^{(C)}$ values in April, May, and June of 2016. The highest Chl-$a^{(C)}$ in 2012–2018 was found in 2015 even though anomalous Chl-$a^{(C)}$ indeed occurred in the spring of 2016. This agrees with the Chl-$a^{(C)}$ maps in 2015 (Fig. 6w). In comparison to Chl-$a^{(C)}$, significant seasonal variation of $K_d^{(C)}(490)$ can be observed ranging between ~0.1–0.3 m^{-1}. The seasonal and interannual variabilities in $K_d^{(C)}(490)$ are similar with those of Chl-$a^{(C)}$. Two peaks of $K_d^{(C)}(490)$ were also observed in June and December, and the lowest $K_d^{(C)}(490)$ in April.

Fig. 10a–10d further characterize and quantify $nL_w(\lambda)$ at the VIIRS bands of 443, 551, and 671 nm for the four stations in the lake. $nL_w(\lambda)$ spectra at Station 1 (Fig. 10a), Station 3 (Fig. 10c), and Station 4 (Fig. 10d) are similar in terms of $nL_w(\lambda)$ magnitudes and their variability. In addition, $nL_w(\lambda)$ at 443, 551, and 671 nm for these three stations change in phase with each other in the period between 2012–2018. At Station 1, values of $nL_w(443)$ and $nL_w(551)$ are close to each other (Fig. 10a). However, $nL_w(443)$ were much lower than $nL_w(551)$ in the summer season at Station 3.

VIIRS-measured $nL_w(\lambda)$ spectra at Station 2 (Fig. 10b) show typical optical features of coastal and inland waters with enhanced $nL_w(\lambda)$ at the wavelengths of 551 and 671 nm. Indeed, $nL_w(551)$ reached ~5 mW cm^{-2} μm^{-1} sr^{-1} in the summer of 2018. In comparison to the other three stations, more interannual variability can be observed at this station. The time series of $nL_w(\lambda)$ at this station shows that the lake water was less turbid with depressed $nL_w(\lambda)$ in the summer of 2015 and 2016. On the other hand, the peak $nL_w(551)$ was ~4 mW cm^{-2} μm^{-1} sr^{-1} in the summers of 2015 and 2016.

Same as results for Chl-$a^{(C)}$ from the entire lake in Fig. 9b, temporal (seasonal and interannual) variability can be found for Chl-$a^{(C)}$ at all four stations (Fig. 10e). In fact, satellite-derived temporal variations in Chl-$a^{(C)}$ at Stations 1, 3, and 4 are generally in phase with each other and follow the Chl-$a^{(C)}$ variation for the entire lake. However, the temporal variation of Chl-$a^{(C)}$ at Station 2 is not the same as those at the other stations. Specifically, Chl-$a^{(C)}$ normally peaks in June and then continuously drops until December at Station 2. In contrast, Chl-$a^{(C)}$ is found to moderately increase from August to December at Stations 1, 3, and 4 for most of the years, even though Chl-$a^{(C)}$ indeed peaks in June at these stations.

VIIRS-derived $K_d^{(C)}(490)$ also show the largest seasonal and interannual changes ranging from 0.1 to 0.5 m^{-1} at Station 2 (Fig. 10f), while seasonal and interannual changes at Stations 1, 3, and 4 (Fig. 10f) were less significant and similar to that of the entire Qinghai Lake (Fig. 9c). In addition, the variation in $K_d^{(C)}(490)$ is not always in phase with the changes at the other three stations. As an example, $K_d^{(C)}(490)$ peaked in the summer months in 2013 and 2016 at Station 2. However, no corresponding peaks were found at the other stations. This suggests that the driving force for $K_d^{(C)}(490)$ changes at Station 2 might not be the same as that in the other parts of the lake.

3.3. *The EOF analyses for Chl-$a^{(C)}$ and $K_d^{(C)}(490)$*

The climatology, seasonal, and international variability data can only provide a static situation for the changes of VIIRS retrievals. Thus, the EOF analyses were conducted with Chl-$a^{(C)}$ and $K_d^{(C)}(490)$ in the lake in order to decompose the spatial and temporal variabilities for these two parameters, and further analyze the variability to identify the dynamic processes.

In the EOF analysis, the pixelwise variances of Chl-$a^{(C)}$ and $K_d^{(C)}(490)$ are first computed after removing the mean values. Next, the spatial variability and the time series variation for the dominant EOF modes are generated and analyzed. Finally, the contribution of each EOF mode to the total variance for the two products in Qinghai Lake is quantified.

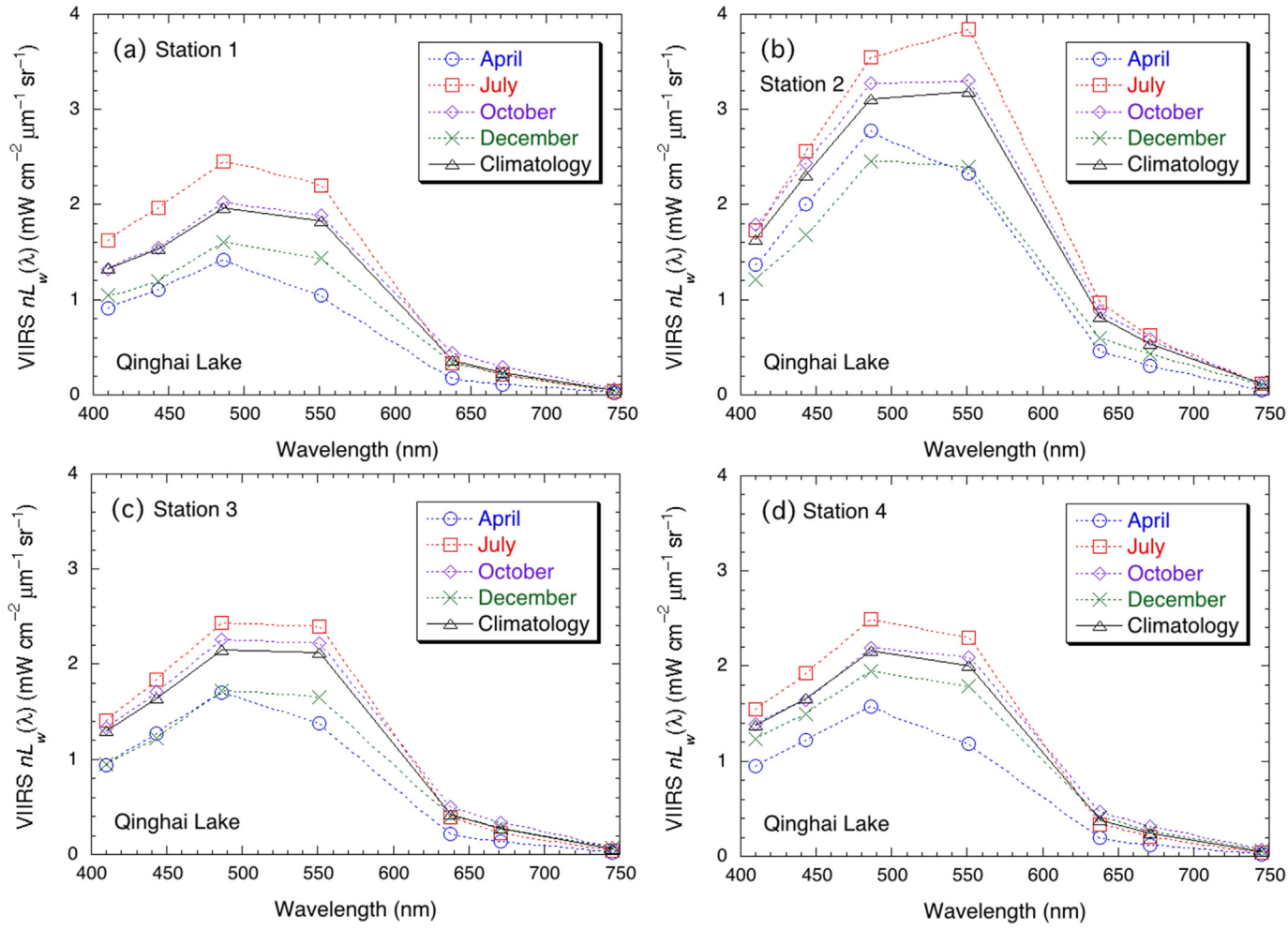

Fig. 8. Satellite-derived $nL_w(\lambda)$ spectra in Qinghai Lake for the climatology (2012–2018) and monthly means in April, July, October, and December at the location of (a) Station 1, (b) Station 2, (c) Station 3, and (d) Station 4.

Fig. 11 shows the spatial distributions of the first (Fig. 11a) and second (Fig. 11b) EOF modes of Chl-a$^{(C)}$. The corresponding temporal changes in 2012–2018 were also computed in Fig. 12a. The first and second modes contribute ~79.1% and ~6.2% of the total variance in Qinghai Lake, respectively. The spatial map of the first mode is generally uniform at ~ +0.3 for most of Qinghai Lake (Fig. 11a). In fact, the time series of the first mode (Fig. 12a) suggests that this mode is dominated by the interannual variability. This temporal variation in the first Chl-a$^{(C)}$ EOF mode was significant in the period of 2012–2016. However, the magnitude was small in the period of 2017–2018.

The values of the spatial pattern in the second Chl-a$^{(C)}$ EOF mode (Fig. 11b) in Qinghai Lake show clear spatial variations. Values are positive in the coastal region of the lake, especially in the western bay regions, while they are slightly positive for most of Qinghai Lake. However, negative values occur in the region of the southern Qinghai Lake. This indicates that the change of Chl-a$^{(C)}$ in the coast does not follow the change in the central lake for this mode. The temporal variation of the second mode (Fig. 12a) shows the seasonal change with positive generally in the summer season and negative between late autumn and spring seasons. The combination of the spatial map and temporal variation for this mode suggests that this mode leads to enhanced Chl-a$^{(C)}$ in the summer and decreased Chl-a$^{(C)}$ in the period of late autumn and spring in coastal regions such as in the western bay. In the central lake, this mode contributes to the drop of Chl-a$^{(C)}$ from the early summer.

The spatial patterns of the first (Fig. 11c) and second (Fig. 11d) $K_d^{(C)}(490)$ EOF modes are shown in Fig. 11. The corresponding time series are shown in Fig. 12b. The first and second EOF modes contribute ~31.5% and ~14.0% total variance of $K_d^{(C)}(490)$ in Qinghai Lake, respectively. Thus, the first mode is the dominant contributor that controls the $K_d^{(C)}(490)$ dynamics in the lake.

The spatial pattern of the first mode is also relatively uniform for Qinghai Lake. High values can be found in the coast of the northern Qinghai Lake (Fig. 11c). The temporal variation for the mode shows that this mode represents the interannual variation in Qinghai Lake. The mode peaks that occurred in October 2012 and June 2016 (Fig. 12b) for the first $K_d^{(C)}(490)$ mode are consistent with $K_d^{(C)}(490)$ peaks in Fig. 9c for the entire lake and in Fig. 10f in the central lake. The mode spatial map and temporal variation show that the first mode is responsible for the interannual variations of $K_d^{(C)}(490)$. On the other hand, the second EOF mode in $K_d^{(C)}(490)$ shows apparent seasonal variation (Fig. 12b) with peaks in the late spring and troughs in the late autumn. Fig. 11d also shows that $K_d^{(C)}(490)$ magnitudes are positive for most of Qinghai Lake. This suggests that the seasonal changes of $K_d^{(C)}(490)$ in the lake are in the same phase. It is also noted that $K_d^{(C)}(490)$ magnitudes are the highest in the western bay region. This is consistent with the seasonal variation of $K_d^{(C)}(490)$ in a variety of lake regions (Fig. 10f) and $K_d^{(C)}(490)$ at Station 2 in the western bay area has the highest seasonal variability (Fig. 10f) in Qinghai Lake.

4. Discussions and conclusion

Located at ~3260 m elevation in the Tibetan Plateau, Qinghai Lake in China has been rarely investigated using satellite remote sensing data in

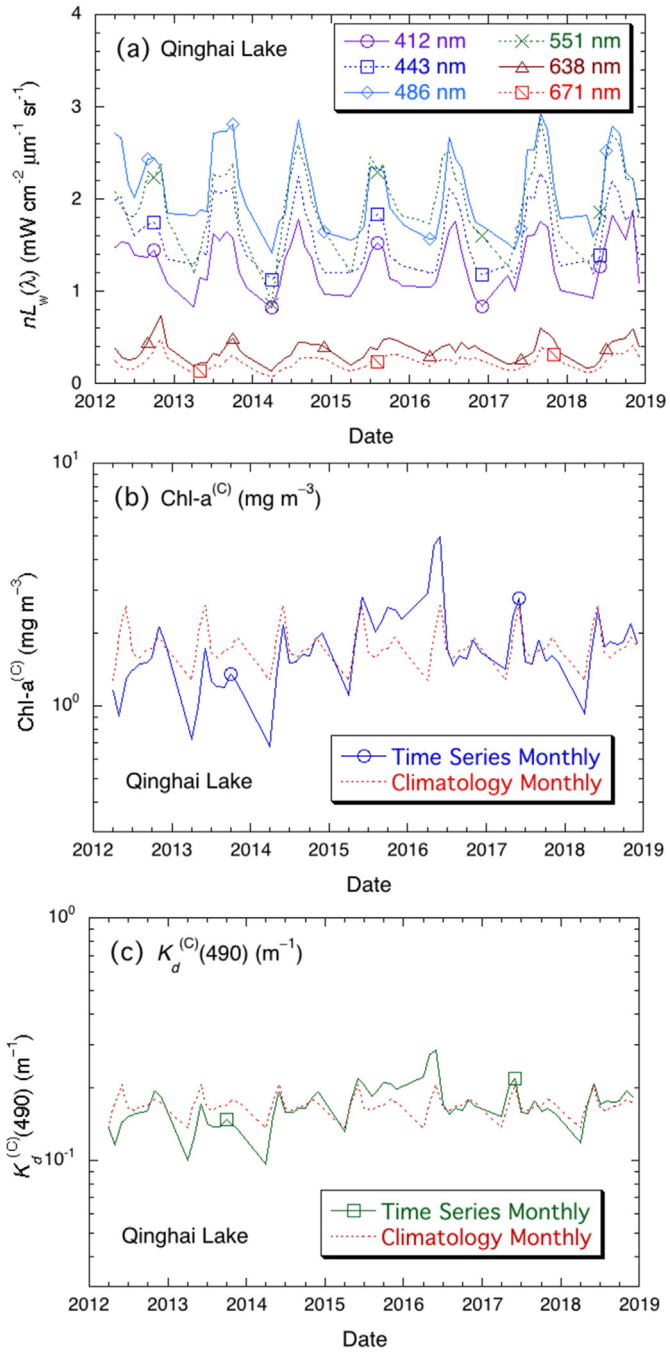

Fig. 9. Satellite-derived temporal variations of water optical properties in the entire Qinghai Lake from 2012–2018 for (a) $nL_w(\lambda)$ at 412, 443, 486, 551, 638, and 671 nm, (b) Chl-a$^{(C)}$, and (c) $K_d^{(C)}$(490). Note that there are no retrievals in the months of January, February, and March.

terms of lake water properties. In this study, VIIRS-SNPP-derived $nL_w(\lambda)$ spectra, Chl-a$^{(C)}$, and $K_d^{(C)}$(490) data in the period of 2012–2018 are used to evaluate water properties over Qinghai Lake. Climatology and seasonal $nL_w(\lambda)$, Chl-a$^{(C)}$, and $K_d^{(C)}$(490) are computed from VIIRS observations for the entire lake. The $nL_w(\lambda)$ retrievals for the various locations in Qinghai Lake are characterized and quantified. For $nL_w(\lambda)$ spectra, we found significant seasonal changes in nL_w(486) and nL_w(551). The highest $nL_w(\lambda)$ at these two bands are usually above ~2.5 and ~2.3 mW cm^{-2} μm^{-1} sr^{-1}, respectively, in the summer (July), while they are below ~1.5 and ~1.2 mW cm^{-2} μm^{-1} sr^{-1}, respectively, in the spring (April) for the entire lake.

There are several studies recently to investigate water clarity, turbidity, and primary production in Qinghai Lake and other lakes in the Tibetan Plateau from MODIS and VIIRS measurements (Liu et al., 2017; Mi et al., 2019; Feng et al., 2019; Wang et al., 2020b). However, results in these studies show that satellite-derived $nL_w(\lambda)$ spectra are usually consistently underestimated in the Tibetan Plateau lakes, which is likely due to the issue of the TOA Rayleigh radiance computations in high-altitude lakes (Wang, 2016; Wang et al., 2020a). Consequently, other satellite-derived water quality products, such as SD, Chl-a, etc., may be unreliable. Indeed, comparison of MODIS-derived and in situ-measured $R_{rs}(\lambda)$ spectra shows that MODIS $R_{rs}(\lambda)$ data at the blue to green bands are ~10–20% consistently biased lower than those from the in situ data in Qinghai Lake (Feng et al., 2019).

In comparison, VIIRS-derived $nL_w(\lambda)$ spectra in this study match quite well with the in situ-measurements. In fact, ratios of the VIIRS-derived and in situ-measured $nL_w(\lambda)$ are close to 1.0 at the blue and green bands (e.g., median ratio of 0.990 for $nL_w(\lambda)$ at 443 nm). This is the first study to provide accurate $nL_w(\lambda)$ retrievals in Qinghai Lake, accurately accounting for the effect of high-altitude lakes in the satellite data processing in the Tibetan Plateau. Furthermore, these VIIRS-derived $nL_w(\lambda)$ spectra are used to quantify and characterize water optical, biological, and biogeochemical variability in Qinghai Lake. Thus, VIIRS-measured $nL_w(\lambda)$ spectra from this study can provide a reference and baseline in order to further develop satellite water property algorithms (i.e., algorithms for biological and biogeochemical products) in Qinghai Lake and the other Tibetan Plateau lakes.

It is noted that VIIRS-calculated Chl-a$^{(C)}$ is used to study variability of water biological property in Qinghai Lake. Chl-a$^{(C)}$ is calculated with VIIRS-derived $nL_w(\lambda)$ spectra in the blue and green bands. Since $nL_w(\lambda)$ spectra are determined by the water inherent optical properties (IOPs) such as amounts of algae, color dissolved organic matter (CDOM), sediment, etc., satellite-derived Chl-a$^{(C)}$ might be less accurate in the complex waters like inland lakes. In Qinghai Lake, however, the trend of Chl-a$^{(C)}$ is the same as from the other study (Feng et al., 2019) using the normalized fluorescence line height (nFLH) (Behrenfeld et al., 2009) and algal bloom index (ABI) (Hu and Feng, 2017). This suggests that VIIRS-calculated Chl-a$^{(C)}$ can indeed be used to evaluate Chl-a variation and trend in Qinghai Lake. It is particularly noted that nFLH, ABI, and Chl-a$^{(C)}$ are three different data sets derived from satellite measurements. They all captured the same phytoplankton biomass trend and particularly the 2016 Chl-a anomaly in Qinghai Lake. The seasonal and interannual variability of Chl-a$^{(C)}$ in this study reflect the variability of real Chl-a in Qinghai Lake from 2012–2018.

Both the interannual and seasonal Chl-a$^{(C)}$ and $K_d^{(C)}$(490) variability in Qinghai Lake are also observed from VIIRS measurements. The lowest Chl-a$^{(C)}$ and $K_d^{(C)}$(490) occur in April, and the year 2015 was found to have the highest Chl-a$^{(C)}$ and $K_d^{(C)}$(490) values in Qinghai Lake between 2012–2018, while the lowest Chl-a$^{(C)}$ and $K_d^{(C)}$(490) were found in 2013. The EOF analysis shows that the first mode represents the interannual Chl-a$^{(C)}$ variability, accounting for ~79.1% of the total Chl-a$^{(C)}$ variance. The second mode represents the seasonal Chl-a$^{(C)}$ variability, accounting for ~6.1% of the total Chl-a$^{(C)}$ variance. For the second Chl-a$^{(C)}$ EOF mode, the spatial variability is notable, showing high seasonal variability in the western coastal region and low seasonal changes at the central lake station. The first and second EOF modes of $K_d^{(C)}$(490) account for ~31.5% and ~14.0% of the total $K_d^{(C)}$(490) variance, respectively. In particular, the seasonal variability in $K_d^{(C)}$(490) is less significant than that of the interannual variability.

There are quite a lot of inland lakes in the Tibetan Plateau. Many lakes over the Tibetan Plateau are highly related to the glaciers and consequently are significantly affected by global warming. These high-altitude lakes are rarely investigated due to their vast area, remote locations, often inclement environments, and logistical difficulties to conduct a field survey. In this study, we show that satellite ocean color remote sensing technology can provide long-term routine observations for global inland lakes including those over the Tibetan Plateau. With future in situ measurements of water optical, biological, and biogeochemical parameters, regional-tuned algorithms (e.g., Chl-a, K_d(490), SD, SPM, IOPs) can

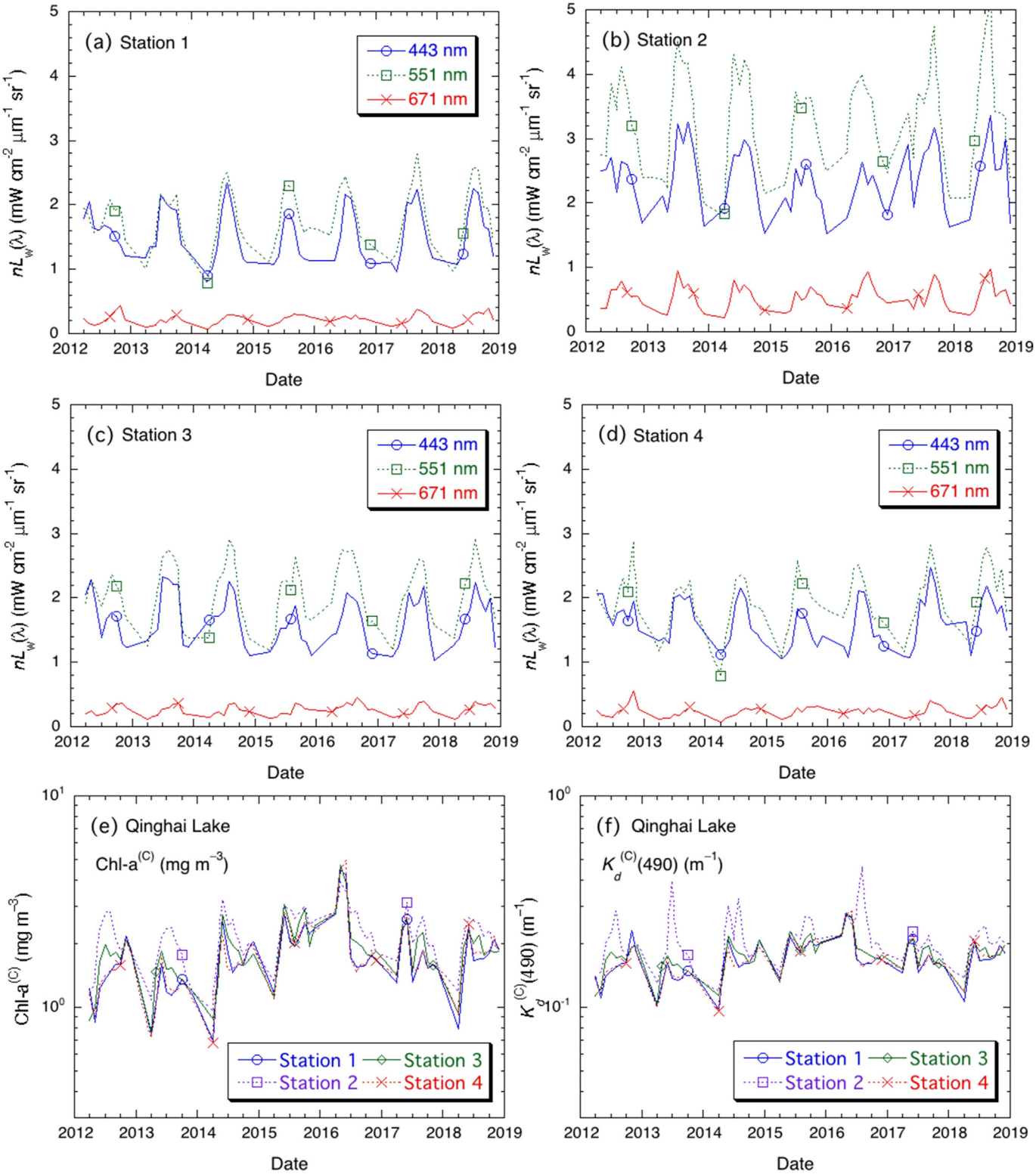

Fig. 10. Satellite-derived temporal variations of $nL_w(\lambda)$ at 443, 551, and 671 nm from 2012–2018 at the location of (a) Station 1, (b) Station 2, (c) Station 3, and (d) Station 4. Temporal variations at Stations 1–4 are also shown for (e) Chl-a$^{(C)}$ and (f) $K_d^{(C)}$(490).

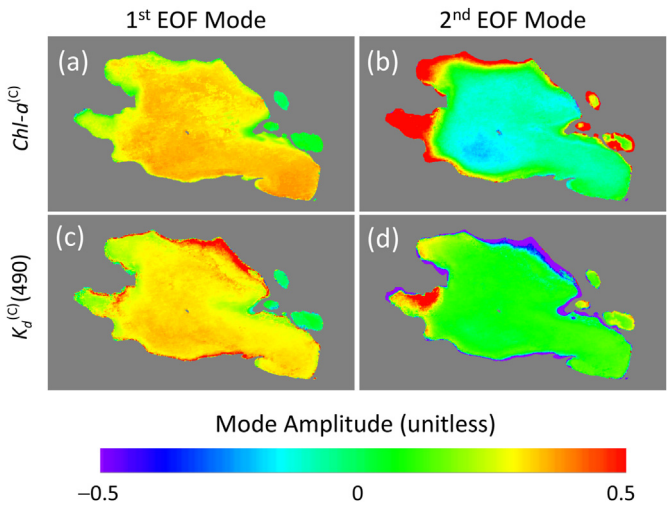

Fig. 11. Maps of the first and second EOF modes in Qinghai Lake for (a and b) Chl-a$^{(C)}$ and (c and d) $K_d^{(C)}(490)$.

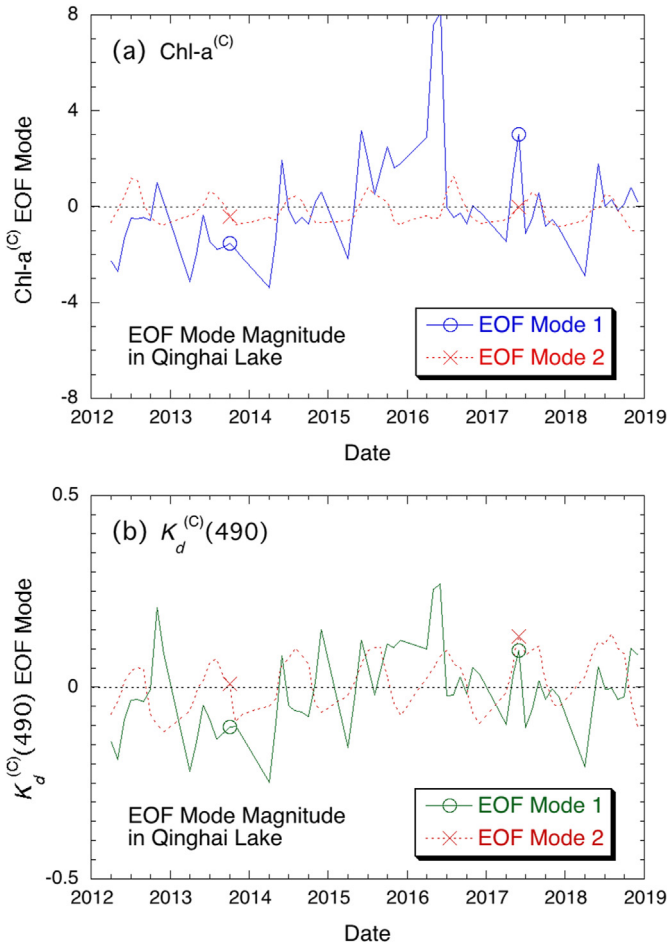

Fig. 12. Time series of the first and second EOF modes for (a) Chl-a$^{(C)}$ and (b) $K_d^{(C)}(490)$.

be developed, evaluated, validated, and eventually applied to satellite ocean color observations. Therefore, satellite ocean color remote sensing not only can provide water property products, but also be used as effective and efficient tools to study these remote high-altitude lakes, monitor their short-term environmental changes, evaluate the long-term variability, and assess the trends of lake environmental changes.

Declaration of competing interest

The authors declare that they have no known competing financial interests or personal relationships that could have appeared to influence the work reported in this paper.

Acknowledgments

This research was supported by the Joint Polar Satellite System (JPSS) funding. The views, opinions, and findings contained in this paper are those of the authors and should not be construed as an official NOAA or U.S. Government position, policy, or decision.

References

Ao, H.Y., Wu, C.X., Xiong, X., Jing, L.D., Huang, X.L., Zhang, K., Liu, J.T., 2014. Water and sediment quality in Qinghai Lake, China: a revisit after half a century. Environ. Monit. Assess. 186, 2121–2133.

Behrenfeld, M.J., Westberry, T.K., Boss, E.S.e.a., 2009. Satellite-detected fluorescence reveals global physiology of ocean phytoplankton. Biogeosciences 6, 779–795. https://doi.org/10.5194/bgd-5-4235-2008.

Cen, Y., Wang, J.N., Zhang, L.F., Zhao, H.Q., 2013. Correlations between water reflectance spectra and chlorophyll concentration in Qinghai Lake. In: IEEE 2013 5th Workshop on Hyperspectral Image and Signal Processing. https://ieeexplore.ieee.org/abstract/document/8080609.

Che, T., Li, X., Jin, R., 2009. Monitoring the frozen duration of Qinghai Lake using satellite passive microwave remote sensing low frequency data. Chin. Sci. Bull. 54, 2294–2299.

El-Habashi, A., Ioannou, I., Tomlinson, M.C., Stumpf, R.P., Ahmed, S., 2016. Satellite retrievals of Karenia brevis harmful algal blooms in the west Florida shelf using neural networks and comparisons with other techniques. Rem. Sens. 8, 377. https://doi.org/10.3390/rs8050377.

Fang, J.M., Li, G.J., Rubinato, M., Ma, G.Q., Zhou, J.X., Jia, G.D., Yu, X.X., Wang, H.N., 2019. Analysis of long-term water level variations in Qinghai Lake in China. Water 11, 2136. https://doi.org/10.3390/w11102136.

Feng, L., Liu, J., Ali, T., Li, J., Li, J., Kuang, X., 2019. Impacts of the decreased freeze-up period on primary production in Qinghai Lake. Int. J. Appl. Earth Obs. Geoinf. 83 https://doi.org/10.1016/j.jag.2019.101915.

Feng, S., Tang, M., Zhou, L., 2000. Level fluctuation in Qinghai Lake during the last 600 years. J. Lake Sci. 12, 205–210.

Goldberg, M.D., Kilcoyne, H., Cikanek, H., Mehta, A., 2013. Joint Polar Satellite System: the United States next generation civilian polar-orbiting environmental satellite system. J. Geophys. Res. Atmos. 118, 13463–13475.

Gordon, H.R., Wang, M., 1994. Retrieval of water-leaving radiance and aerosol optical-thickness over the oceans with seawifs - a preliminary algorithm. Appl. Optic. 33, 443–452.

Hansen, J., Ruedy, R., Sato, M., Lo, K., 2010. Global surface temperature change. Rev. Geophys. 48 https://doi.org/10.1029/2010rg000345.

Hu, C., Feng, L., 2017. Modified MODIS fluorescence line height data product to improve image interpretation for red tide monitoring in the eastern Gulf of Mexico. J. Appl. Remote Sens. Environ. 11 https://doi.org/10.1117/1.JRS.11.012003.

Hu, C.M., Lee, Z.P., Ma, R.H., Yu, K., Li, D.Q., Shang, S.L., 2010. Moderate resolution imaging spectroradiometer (MODIS) observations of cyanobacteria blooms in Taihu Lake, China. J Geophys Res-Oceans 115. https://doi.org/10.1029/2009jc005511.

Hu, C., Lee, Z., Franz, B., 2012. Chlorophyll a algorithms for oligotrophic oceans: a novel approach based on three-band reflectance difference. J Geophys Res-Oceans 117. https://doi.org/10.1029/2011jc007395.

IOCCG, 2010. In: Wang, M. (Ed.), Atmospheric Correction for Remotely-Sensed Ocean-Colour Products, Reports of International Ocean-Color Coordinating Group, No. 10. IOCCG, Dartmouth, Canada, p. 77.

Jin, Z.D., You, C.F., Wang, Y., Shi, Y.W., 2010. Hydrological and solute budgets of Lake Qinghai, the largest lake on the Tibetan Plateau. Quat. Int. 218, 151–156.

Lee, Z.P., Carder, K.L., Arnone, R.A., 2002. Deriving inherent optical properties from water color: a multiband quasi-analytical algorithm for optically deep waters. Appl. Optic. 41, 5755–5772.

Li, W.Q., Cardellach, E., Fabra, F., Ribo, S., Rius, A., 2018. Lake level and surface topography measured with spaceborne GNSS-reflectometry from CYGNSS mission: example for the lake Qinghai. Geophys. Res. Lett. 45, 13332–13341.

Liu, C., Zhu, L., Wang, J., Qiao, B., Ju, J., Huang, L.L., 2017. Remote sensing-based estimation of lake water clarity on the Tibetan plateau. Prog. Geogr. 36, 597–609.

Mi, H., Fagherazzi, S., Qiao, G., Hong, Y., Fichot, C.G., 2019. Climate change leads to a doubling of turbidity in a rapidly expanding Tibetan lake. Sci. Total Environ. 688, 952–959. https://doi.org/10.1016/j.scitotenv.2019.06.339.

O'Reilly, J.E., Maritorena, S., Mitchell, B.G., Siegel, D.A., Carder, K.L., Garver, S.A., Kahru, M., McClain, C., 1998. Ocean color chlorophyll algorithms for SeaWiFS. J. Geophys. Res. C Oceans 103, 24937–24953.

Shen, F., Kuang, D., 2002. Remote sensing investigation and survey of Qinghai Lake in the past 25 years. J. Lake Sci. 15, 289–296.

Shi, W., Zhang, Y., Wang, M., 2018. Deriving total suspended matter concentration from the near-infrared-based inherent optical properties over turbid waters: a case study in Lake Taihu. Rem. Sens. 10, 333. https://doi.org/10.3390/rs10020333.

Shi, W., Wang, M., Zhang, Y., 2019. Inherent optical properties in Lake Taihu derived from VIIRS satellite observations. Rem. Sens. 11, 1426. https://doi.org/10.3390/rs11121426.

Tang, L.Y., Duan, X.F., Kong, F.J., Zhang, F., Zheng, Y.F., Li, Z., Mei, Y., Zhao, Y.W., Hu, S.J., 2018. Influences of climate change on area variation of Qinghai Lake on Qinghai-Tibetan plateau since 1980s. Sci. Rep. 8 https://doi.org/10.1038/s41598-018-25683-3.

Wan, W., Li, H., Xie, H.J., Hong, Y., Long, D., Zhao, L.M., Han, Z.Y., Cui, Y.K., Liu, B.J., Wang, C.G., Yang, W.T., 2017. A comprehensive data set of lake surface water temperature over the Tibetan Plateau derived from MODIS LST products 2001-2015. Sci Data 4. https://doi.org/10.1038/sdata.2017.95.

Wang, M., 2007. Remote sensing of the ocean contributions from ultraviolet to near-infrared using the shortwave infrared bands: simulations. Appl. Optic. 46, 1535–1547.

Wang, M., 2016. Rayleigh radiance computations for satellite remote sensing: accounting for the effect of sensor spectral response function. Optic Express 24, 2414–2429.

Wang, M., Franz, B.A., 2000. Comparing the ocean color measurements between MOS and SeaWiFS: a vicarious intercalibration approach for MOS. IEEE Trans. Geosci. Rem. Sens. 38, 184–197.

Wang, M., Isaacman, A., Franz, B.A., McClain, C.R., 2002. ocean color optical property data derived from the Japanese ocean color and temperature scanner and the French polarization and directionality of the earth's reflectances: a comparison study. Appl. Optic. 41, 974–990.

Wang, M., Shi, W., Watanabe, S., 2020a. Satellite-measured water properties in high altitude Lake Tahoe. Water Res. 178, 115839. https://doi.org/10.1016/j.watres.2020.115839.

Wang, M., Liu, X., Tan, L., Jiang, L., Son, S., Shi, W., Rausch, K., Voss, K., 2013a. Impacts of VIIRS SDR performance on ocean color products. J. Geophys. Res. Atmos. 118, 10347–10360.

Wang, M., Nim, C.J., Son, S., Shi, W., 2012. Characterization of turbidity in Florida's Lake Okeechobee and Caloosahatchee and st. Lucie estuaries using MODIS-aqua measurements. Water Res. 46, 5410–5422.

Wang, M., Shi, W., 2007. The NIR-SWIR combined atmospheric correction approach for MODIS ocean color data processing. Optic Express 15, 15722–15733.

Wang, M., Shi, W., Tang, J.W., 2011. Water property monitoring and assessment for China's inland Lake Taihu from MODIS-Aqua measurements. Remote Sens. Environ. 115, 841–854.

Wang, M., Son, S., 2016. VIIRS-derived chlorophyll-a using the ocean color index method. Remote Sens. Environ. 182, 141–149.

Wang, M., Son, S., Harding Jr., L.W., 2009. Retrieval of diffuse attenuation coefficient in the Chesapeake Bay and turbid ocean regions for satellite ocean color applications. J. Geophys. Res. 114, C10011. https://doi.org/10.1029/2009JC005286.

Wang, M., Son, S., Zhang, Y., Shi, W., 2013b. Remote sensing of water optical property for China's inland Lake Taihu using the SWIR atmospheric correction with 1640 and 2130 nm bands. IEEE J. Sel. Topics Appl. Earth Observ. Remote Sens. 6, 2505–2516.

Wang, S.L., Li, J.S., Zhang, B., Lee, Z.P., Spyrakos, E., Feng, L., Liu, C., Zhao, H.L., Wu, Y.H., Zhu, L.P., Jia, L.M., Wan, W., Zhang, F.F., Shen, Q., Tyler, A.N., Zhang, X.F., 2020b. Changes of water clarity in large lakes and reservoirs across China observed from long-term MODIS. Remote Sens. Environ. 248 https://doi.org/10.1016/j.rse.2020.111984.

Wang, X., Li, T., Hu, J.C., 2005. Analysing Surface Water Optical Properties of Qinghai Lake. Journal of Ocean Technology 24, 50–54.

Xiao, F., Ling, F., Du, Y., Feng, Q., Yan, Y., Chen, H., 2013. Evaluation of spatial-temporal dynamics in surface water temperature of Qinghai Lake from 2001 to 2010 by using MODIS data. J. Arid Land 5, 452–464.

Xu, Z.X., Gong, T.L., Li, J.Y., 2008. Decadal trend of climate in the Tibetan Plateau - regional temperature and precipitation. Hydrol. Process. 22, 3056–3065.

Yao, W., Shi, J., Qi, H., Yang, J., Jia, l., Pu, J., 2011. Study on the phytoplankton in Qinghai Lake during summer of 2006—2010. J. Freshwater Fisheries 41, 24–30.

Yu, X., Lee, Z., Shen, F., Wang, M., Wei, J.W., Jiang, L., Shang, Z., 2019. An empirical algorithm to seamlessly retrieve the concentration of suspended particulate matter from water color across ocean to turbid river mouths. Remote Sens. Environ. 235 https://doi.org/10.1016/j.rse.2019.111491.

Zhang, G.Q., Xie, H.J., Duan, S.Q., Tian, M.Z., Yi, D.H., 2011. Water level variation of Lake Qinghai from satellite and in situ measurements under climate change. J. Appl. Remote Sens. 5 https://doi.org/10.1117/1.3601363.

Zhang, G.Q., Xie, H.J., Kang, S.C., Yi, D.H., Ackley, S.F., 2011b. Monitoring lake level changes on the Tibetan Plateau using ICESat altimetry data (2003-2009). Remote Sens. Environ. 115, 1733–1742.

Zhang, R.Y., Ludwig, A., Zhang, C.F., Tong, C., Li, G.G., Tang, Y.T., Peng, Z.G., Zhao, K., 2015. Local adaptation of gymnocypris przewalskii (cyprinidae) on the Tibetan plateau. Sci. Rep. 5 https://doi.org/10.1038/srep09780.

Zhou, H., Hu, J.C., Li, T., Wang, X., 2005. The analysis of water color element absorb spectral characteristic in Qinghai Lake - yellow substance, De-pigment particles and phytoplankton pigments. J. Ocean Technol. 24, 55–58.

Zhu, J.H., Zhou, H.L., Han, B., Li, T.J., 2016. Feature analysis of phytoplankton pigments in Qinghai Lake. In: IEEE Conference Oceans 2016 - Shanghai, pp. 1–7. https://doi.org/10.1109/OCEANSAP.2016.7485739.